Linking thermal and rate behavior with fabric and mineralogy of clayey shear zones: Experimental investigation on the El Forn landslide (Andorra)

Carolina Seguí[a,*], Esperança Tauler[b], Tomasz Hueckel[c], Manolis Veveakis[c]

[a] *RWTH Aachen University, Aachen, Germany*
[b] *University of Barcelona, Barcelona, Spain*
[c] *Duke University, Durham, NC, USA*

Abstract

Thermal triaxial tests were carried out on remolded material of core samples of the shear zone of a deep-seated landslide, the El Forn landslide (Andorra). With the thermal triaxial tests, we have obtained thermal and rate sensitivities of the material outside and inside the shear band. Moreover, micro-scale tests were carried out, such as XRPD, SEM-EDS, MicroCT, and plasticity index. The results show that the material inside the shear band has higher thermal sensitivity than outside the shear band. These results are related to the material's fabric, porosity, and plasticity index. The rate sensitivity value is the same for the samples outside and inside the shear band, being able to correlate the rate sensitivity with the mineralogy content of the material. This study, thus, aims to understand the mechanical behavior of the material within a shear zone by correlating the thermal and rate sensitivity with the microstructure and mineral phases present in the material.

*Corresponding author: C. Seguí
Email address: `segui@gut.rwth-aachen.de` (Carolina Seguí)

Keywords: Thermal sensitivity, Rate sensitivity, Thermal triaxial, Micro-structure, Mineralogy, Shear zone

1. Introduction

This paper presents the behavior of clayey materials, outside and inside the shear zone, of a deep-seated landslide by linking the thermal and rate sensitivities with the fabric and mineralogy of the material. The effect of friction/shearing in a clayey layer with continuous creeping changes the orientation of the mineral particles, thus affecting the material's mechanical behavior by decreasing its friction coefficient and increasing the weakness of the material (Anderson, 1980; Lachenbruch, 1980; Mase & Smith, 1985; Rice, 2006; Vardoulakis, 2002b; Voight & Faust, 1982). Moreover, changes in the loading rate on the material also affect the mechanical behavior of the shear layer (Song *et al.*, 2014; Wang *et al.*, 2017; Rattez & Veveakis, 2020; Rattez *et al.*, 2018), depending on its mineralogy content. The effect of thermal and loading rate behavior of geomaterials, especially in clays, has been explored in the fields of fault mechanics (i.e., earthquakes) (Rice, 2006; Chambon *et al.*, 2002; Tesei *et al.*, 2012; Kohli & Zoback, 2013; Veveakis *et al.*, 2010; Alevizos *et al.*, 2014; Veveakis *et al.*, 2014; Poulet *et al.*, 2014), nuclear waste disposal (Hueckel & Baldi, 1990; Hueckel & Borsetto, 1990; Hueckel & Pellegrini, 1991, 1992; Del Olmo *et al.*, 1996; Hueckel *et al.*, 2009; Monfared *et al.*, 2014; Gens *et al.*, 2018; Laloui, 2001), and landslides (Vardoulakis, 2002a,b; Veveakis *et al.*, 2007; Ciantia & Hueckel, 2013; Seguí *et al.*, 2020; Seguí & Veveakis, 2021; Goren & Aharonov, 2007), as well as energy applications (Veveakis & Regenauer-Lieb, 2015; Laloui & Cekerevac, 2003;

Sari *et al.*, 2020).

In fault mechanics and earthquake engineering, the effect of rate sensitivity of the material has been tested to understand the mechanics of the gauge material (Chambon *et al.*, 2002; Tesei *et al.*, 2012; Kohli & Zoback, 2013; Sulem *et al.*, 2011). In nuclear waste disposal, the effect of thermal loading has been an important parameter in studying the material's behavior due to the low permeability of some clays and to understanding how the material responds when is under very high temperatures (Hueckel & Baldi, 1990; Hueckel & Borsetto, 1990; Hueckel & Pellegrini, 1991, 1992; Del Olmo *et al.*, 1996; Hueckel *et al.*, 2009; Monfared *et al.*, 2014; Gens *et al.*, 2018). In landslides, the effect of rate sensitivity has been considered for the shear band material due to the changes in groundwater levels (seasonal variations, reservoir levels, etc.). Moreover, several authors consider the effect of temperature on landslides due to shearing movement increases the temperature in the material due to friction. The increase of temperature in the material modifies the friction coefficient of the shear band's material (Vardoulakis, 2002b; Veveakis *et al.*, 2007; Pinyol & Alonso, 2010; Alonso *et al.*, 2016; Seguí *et al.*, 2020; Seguí & Veveakis, 2021, 2022), as well as the effects of degradation of the material due to weathering, which leads to slope instabilities (Ciantia & Hueckel, 2013; Cecinato *et al.*, 2010; Cecinato & Zervos, 2012).

This study focuses on the role of thermal sensitivity due to the fabric of the material, especially in clays or clayey materials. Previous studies have been performed, to have a better understanding of the behavior of clayey materials. In particular, Seguí & Veveakis (2021) presented the results of thermal sensitivity in black shales of the Silurian, outside and inside the shear band, of a deep-seated landslide. The results showed different values of thermal sensitivity, being higher inside the shear band where the phyllosilicates are completely aligned face-face (Seguí *et al.*, 2021). In addition, Del Olmo *et al.* (1996) analyzed the thermomechanical properties of Spanish and Boom clays at temperatures close to nuclear waste disposal, finding that the material is thermal softening and strain hardening. In that study, Del Olmo *et al.* (1996) already discussed that the effect of the microstructure could affect the microfractures and dehydration of the material, leading to those thermomechanical results. Later, Hueckel *et al.* (2009) performed thermal tests on Spanish clay obtaining thermal softening and plastic strain hardening of the material (i.e., reduction of strength with increasing temperature). In their study Hueckel *et al.* (2009) discuss that the decrease of internal friction while the increasing temperature is related to the contacts of the particles, as it affects the water absorbed by the particles depending on how they are connected (face-face, face-edge, edge-edge).

In addition, the present work also analyzes the interplay between the loading rate sensitivity of a clayey material related to the mineralogy content. Previous studies have presented results of the behavior of clayey materials under different loading rates. Seguí & Veveakis (2021) presented the results of rate sensitivity for black shales of the Silurian outside and inside the shear band of a deep-seated landslide. They obtained the same values of rate sensitivity for all the samples tested, thus suggesting that the rate sensitivity depends on the sample's mineralogy rather than the orientation of the mineral particles. In the mid-1970s, Leinenkugel (1976) performed velocity stepping tests on remolded kaolin clay, obtaining the rate hardening of the material and its law. Later, Ikari *et al.* (2009) performed laboratory tests on synthetic montmorillonite gauge through velocity stepping in a biaxial apparatus, obtaining as well rate hardening of the material. Finally, Samuelson & Spiers (2012) performed laboratory tests in illite simulated fault gouge through velocity stepping in a direct shear machine, obtaining rate hardening of the material (i.e., strength increase of the material, when the loading rate increases).

Several studies have presented constitutive models combining the effects of rate hardening and thermal softening. Firstly, Hueckel & Borsetto (1990) postulated the constitutive equations of the plastic behavior of clay and shales from the experiments performed previously by Hueckel & Baldi (1990). These constitutive equations express the counterbalancing effects of thermal softening and plastic strain hardening. Afterward, Vardoulakis (2002b) presented a constitutive model of the thermo-viscoplastic coupling in clayey gouges. Vardoulakis (2002b) showed the results of thermal softening from Hicher (1974), rate hardening of Leinenkugel (1976), and explained the importance that both effects must counterbalance. Later, Veveakis *et al.* (2007), Seguí *et al.* (2020), and Seguí & Veveakis (2021) continued this line of Vardoulakis (2002b) in deep-seated landslides strengthening the thermal sensitivity and rate hardening coupling and proving the assumption by performing laboratory experiments on the gauge of a deep-seated landslide. Moreover, Hueckel *et al.* (2009) presented an in-depth study of the thermal failure in saturated clays combining mathematical modeling with experimental data. The authors, again, showed the importance of counterbalancing the effects of thermal softening and rate hardening of the clayey material.

The validation of the aforementioned counterbalanced constitutive laws has been presented and discussed previously by the authors (Seguí & Veveakis, 2021). They presented experimental results of thermal and rate sensitivities of the Silurian black shales of the El Forn landslide (Andorra). Moreover, the authors have previously performed on the same Silurian shales mineralogical tests by X-Ray Powder Diffraction (XRPD), textural analysis by Scanning electron microscope with energy-dispersive X-ray spectroscopy (SEM-EDS), porosity by Micro X-ray computed tomography scanner (MicroCT), and plasticity index (Seguí *et al.*, 2021). However, the link between the thermal and rate sensitivity behavior with the material's mineral content and the internal structure has not been examined and discussed yet. Therefore, this paper presents an in-depth study of experimental tests in a thermal-triaxial machine on the same black shales of the Silurian period from core samples inside and outside the shear band of the El Forn landslide (Andorra), and the micro-scale tests performed as well (Seguí *et al.*, 2021). We have merged all the results and presented them in this paper to understand and link the differences obtained from the thermal and rate sensitivity tests with the fabric and mineralogy of the samples. This paper aims to shed light on the mechanisms present in shear bands containing clayey materials and understand why the material behaves as softening or hardening when the temperature and the loading rate change.

2. Materials

In this work, we study the core samples of the inside and outside the shear band of the lobe Cal Ponet-Cal Borronet inside the large El Forn landslide (Andorra) (Fig. 1 an S10 borehole). This lobe is approximately $1Mm^3$ of rock mass sliding as a rigid block (i.e., translational/rotational) with an average velocity of $2cm/year$ (Corominas *et al.*, 2014) (Fig. 1b). The samples we test in this study were preserved from the S10 borehole performed at the Cal Ponet-Cal Borronet lobe in 2007 (Fig. 1c). In Fig. 1c can be seen that the samples we study are fully saturated in water, indicated by the information from piezometers installed in the borehole (EuroconsultSA, 2017). The shear band of the lobe and its surroundings are formed by black shales from the Silurian (Clariana, 2004). The core samples studied are located between 27 and 30m depth (Figure 1b,c), being its shear band located at 29-29.5m depth (Fig. 1b,c) (Seguí *et al.*, 2021). In this study, we will divide each sample every half a meter of the vertical depth, thus at every $0.5m$, characterizing six samples to see the evolution in-depth of the mineralogy, orientation, porosity, and plasticity index.

The core samples have been studied at the micro-scale to determine their mineralogy composition, the fabric (i.e., the orientation of the minerals), the porosity, and its plastic and liquid limits. At the meso-scale, we determine the critical-state line of the material (black shales of the Silurian), the friction coefficient at the critical state, and the thermal and rate sensitivities.

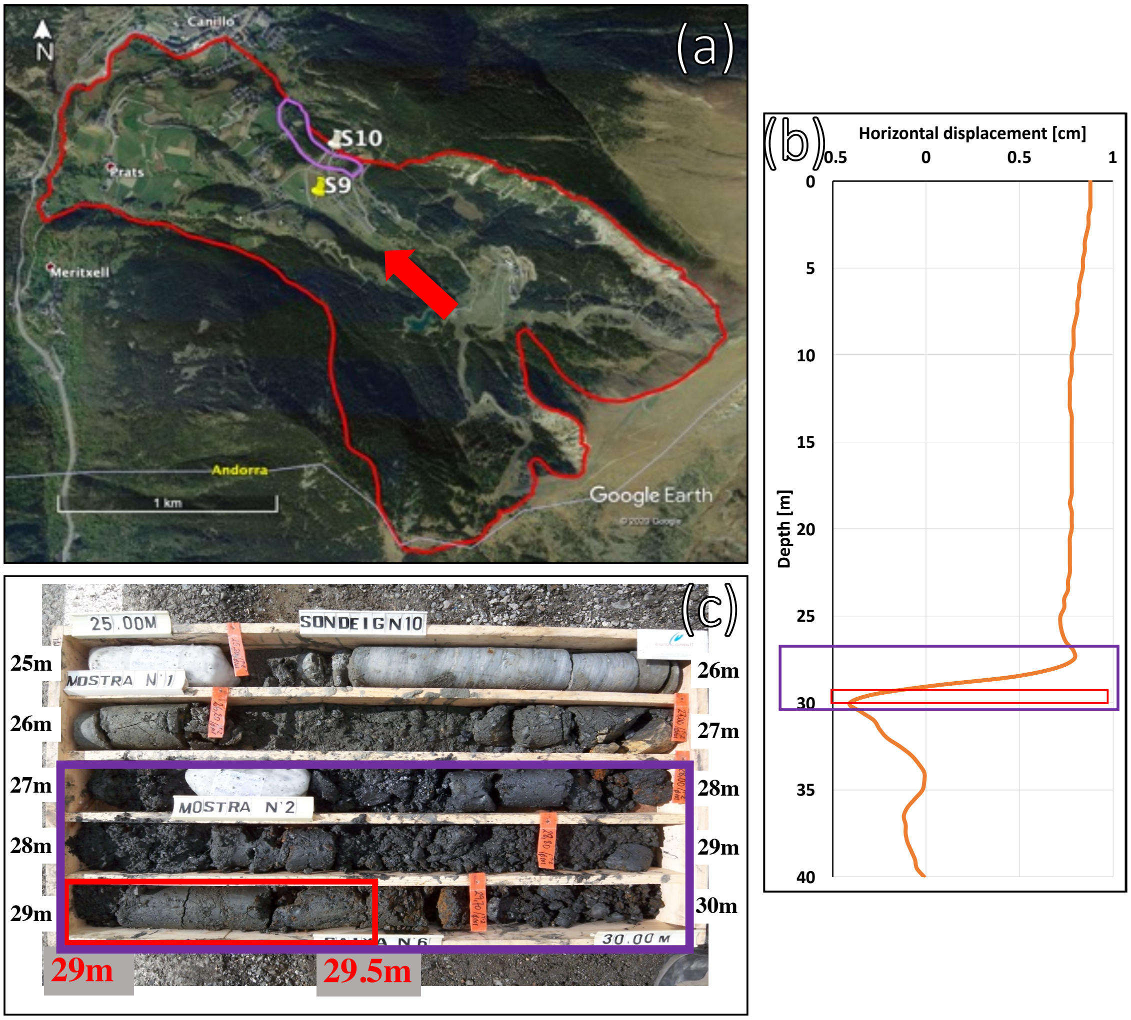

Figure 1: The deep-seated landslide of El Forn in Andorra. (a) Google Earth image highlighted the large El Forn landslide (red) and the Cal Ponet-Cal Borronet lobe (purple), with the S9 and S10 boreholes. (b) Extensometer displacement data profile (in-depth) of the S10 borehole. The data is from April to June 2017 (EuroconsultSA, 2017). (c) Core samples preserved of the S10 borehole performed in 2007, including the shear band of the Cal Ponet-Cal Borronet lobe and its center highlighted in a red rectangle. The samples tested in this study are highlighted by a purple rectangle.

3. Micro-scale characterization of the shearing zone material

In this section, we explain the technical features of the micro-scale tests performed on the black shales of the Silurian from the Cal Ponet - Cal Borronet lobe. The micro-scale tests performed on the samples are: XRPD to obtain the mineralogy, SEM-EDS to see the fabric and orientation of the mineralogy, MicroCT for the porosity, and Plasticity Index as the mechanical property of the samples.

3.1. X-Ray Powder Diffraction

Samples studied in XRPD needed to be crushed in an agate mortar until the rock reduces its particle size below $40\mu m$, ending as fine powder that does not scrape between the fingers. XRPD data were collected with Panalytical X'Pert PRO MPD X-ray diffractometer, with monochromatized incident $CuK\alpha 1$ radiation at $45kV$ and $40mA$, equipped with a PS detector with an amplitude of 2.113°. Patterns were obtained by scanning randomly-oriented powder particles from 4° to 80° (2θ). Datasets were obtained using a scan time of 50 seconds at a step size of 0.017° (2θ) and a variable automatic divergence slit. The identification of minerals was achieved by comparing XRPD with the ICDD database (2007 release) using Diffrac plus Evaluation software (Bruker, 2007). Quantitative mineral phase analyses were obtained by full refinement profile using XRPD and the software TOPAS V4.2 (2009) (Coelho, 2000).

3.2. Scanning Electron Microscope with Energy-Dispersive X-Ray Spectroscopy

To study samples in SEM-EDS, we have created thin polished thin sections from the core samples. The sample preparation procedure of a thin section includes cutting a $1000mm^3$ cubical or prismatic sample from a cylindrical core of undisturbed material retrieved at a depth between $27m$ to $30m$ (shear band). A cubical sample is first included in epoxy resin and then attached to a glass sample holder -on one side-, to cut a slice of $50\mu m$ thick on which SEM observations will be performed. Finally, a metallographic polishing -under dry conditions-, is carried out to obtain the flat surface needed for EDS analyses. Morphology and microtextural features of the studied samples were examined with Nikon Eclipse LV100 POL microscope and ESEM Quanta 200 FEI, XTE 325/D8395 scanning electron microscope with energy-dispersive X-ray spectroscopy (SEM-EDS).

3.3. Micro X-Ray Computed Tomography Scanner

MicroCT tests were performed on the studied core samples. Multiple tests have been carried out to ensure the representativeness of the samples and repeatability of the results. The porosity of the studied samples was examined on chips of original core rock (order of *cm*) with a Nikon XTH 225 ST, which is a high-resolution X-Ray computed tomography scanner. With this scanner, 2-D and 3-D images of inside and outside the sample are obtained by projection of an X-Ray beam through the sample and the sample's interaction with the beam via radiography/X-Ray image. The X-ray source used in the tests performed is the $225kV$ UltraFocus Reflection Based Signal and Tungsten Target (Spot Size $3\mu m$) with a Max Power of $200W$. The detector used is the Perkin Elmer 1620 AN3 CS CT. The X-ray filter used is a $0.5mm$ thick copper filter. We have used the Avizo Software (TJP, 2015) to post-process the 2-D Micro-CT images. The 3-D reconstruction and the quantification of the matrix and the porosity, separately, have been performed by segmenting the 2-D images (i.e., separating the pores from the matrix using a gradient threshold method).

Once the segmentation is successful (i.e., the contacts between the matrix and the pores are well defined as well as the contour of the sample from the background), the quantification of the volumes is automatic by the Avizo Software. To quantify the volume of pores, and the volume of the matrix, the software uses the voxel size of the image, the 3-D reconstruction, and the segmentation. The technical features of MicroCT Scanner images include resolution (voxel size) between 0.0265 and $0.0443mm$, detector 2000x2000 pixels with each pixel spaced at $200\mu m$, 2500 projections, angle steps of $0.144°$, and X-Ray energy of $190kV$.

3.4. Plasticity Index

The plasticity index has been obtained for the studied samples. For each sample, we have performed three tests for reliable results. First, a Plastic Limit test was performed, and second a Liquid Limit test using Casagrande's liquid limit device. Both tests, liquid limit and plastic limit, have been performed following the standard approach in soil mechanics (Das, 1941). The geological material used for the tests was the powder size of the core samples (μm) mixed with small flakes (mm).

4. Meso-scale characterization of the shearing zone material

In this section, we explain the methodology followed to carry out a proper meso-scale characterization of the core samples to test in the thermal triaxial apparatus. Firstly, we define the protocol performed to remold the core samples from the S10 borehole. Then, we explain the experimental protocol we have carried out to obtain the optimal confining pressure to perform the thermal and rate tests, the critical-state line, cohesion, and the angle of friction coefficient of the material (black shales of the Silurian).

4.1. Remolding of the samples

The core samples from the landslide were in a dry state due to their preservation (Fig. 1c). Therefore, they have been healing in a humidity chamber for three months at 85% humidity. The sample's grain size has been defined by three main sizes: chips from dm to cm, flakes from cm to mm, and powder size as μm. The material chosen to test in the triaxial has been the powder size mixed with mm flakes (Fig. 2a). The samples were mixed with water (Fig. 2b) to reach an average humidity of 70% at a room humidity of 45% and a room temperature of $20°C$. The saturated material was placed in cylindrical molds of $35mm$ in diameter and $85mm$ height by applying compaction to reduce voids once the sample dried. The molds with the soil have been drying for 48 hours in the oven at a temperature of $50°C$. Afterward, they have been 6 hours at room temperature to cool down and removed the molds to let the sample reach room temperature and dry for 24 hours before cutting and preserving them, covered in a plastic bag, in the fridge until their test. The samples tested in the thermal triaxial machine have a size of $35mm$ in diameter and a height between $65 - 70mm$ height (Fig. 2b), with an average sample temperature of $20°C$ and 40% humidity, and an average room temperature of $21°C$ and 50% humidity.

The remolded samples have been tested in a customized thermal triaxial machine (Fig. 2d,e,f) to characterize the thermal and rate sensitivities of the Silurian shales of the inside and outside the shear band. The core samples have been tested with the same characterization (i.e., every half a meter depth) as the micro-scale tests.

4.2. Experimental protocol

For the tests performed on all the samples in the thermal triaxial machine, we have always followed the same steps in the same order to have consistency in the results and repeatability. The cylindrical samples, $38mm$ diameter and $65-70mm$ height (Fig. 2c), are not consolidated after being remolded at the reported field humidity. Therefore, we have first performed a triaxial compression on the samples outside the shear band at varying pressures between $50-700kPa$ in undrained conditions (Fig. 3a). With the data of the tests performed, we can calculate the mean effective stress as $p' = \frac{\sigma_1}{3} + 2\frac{\sigma_3}{3}$, being $\sigma_1 = \frac{LoadCell}{SampleArea}$, and σ_3 the confinement pressure. We also calculate the corrected deviatoric stress as $q = \sigma_1 - \sigma_3$. To obtain the critical state line of the material (Fig.3b), we plot the calculated values of p' and q of each confinement pressure and calculate the linear interpolation between the points. The equation of the critical state line is presented in Fig.3b. The slope, M_{cs}, of the critical state line is 1.3, and the friction angle of the material at critical state is calculated as $M_{cs} = \frac{q}{p'} = \frac{6sin\phi_{cs}}{3-sinn\phi_{cs}}$, and has a value of 32.52°, and a cohesion of $213.3kPa$ (Santamarina & Cho, 2001).

Once the material has been characterized, we have tested all the samples (outside and inside the shear band) to determine their rate and thermal sensitivities. As the material was limited, due to the samples being from the S10 borehole (Fig. 1c) and only being able to remold them twice, we have performed thermal and rate sensitivity tests at a critical state in each test as follows:

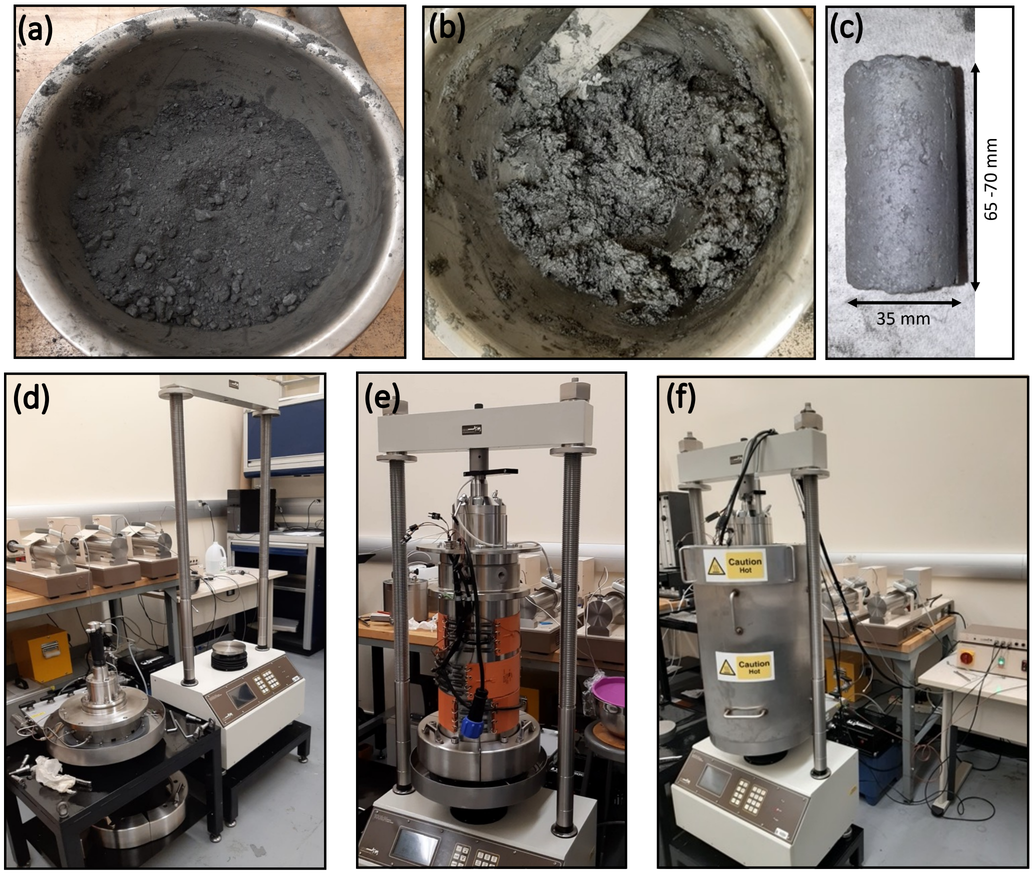

Figure 2: Remolding of the samples and the customized thermal triaxial machine. (a) Dry state of the material of the S10 borehole after being in the humidity chamber. The size of the material is powder size mixed with *mm* flakes. (b) Material of Fig. 2a saturated in water with an approximate humidity of 70%. (c) The final shape of the remolded sample (Fig. 2a,b) after being dried in the oven and cut. This figure represents the samples tested in the customized thermal triaxial machine. (d) The base of the cell, the triaxial frame, and the three pumps. (e) The thermal cell in the triaxial frame, where the orange pads are the heating sources to increase the temperature in the cell and the sample. (f) Thermal triaxial machine with the protector case for the thermal tests and the sensors controller for the piston and temperature on the right.

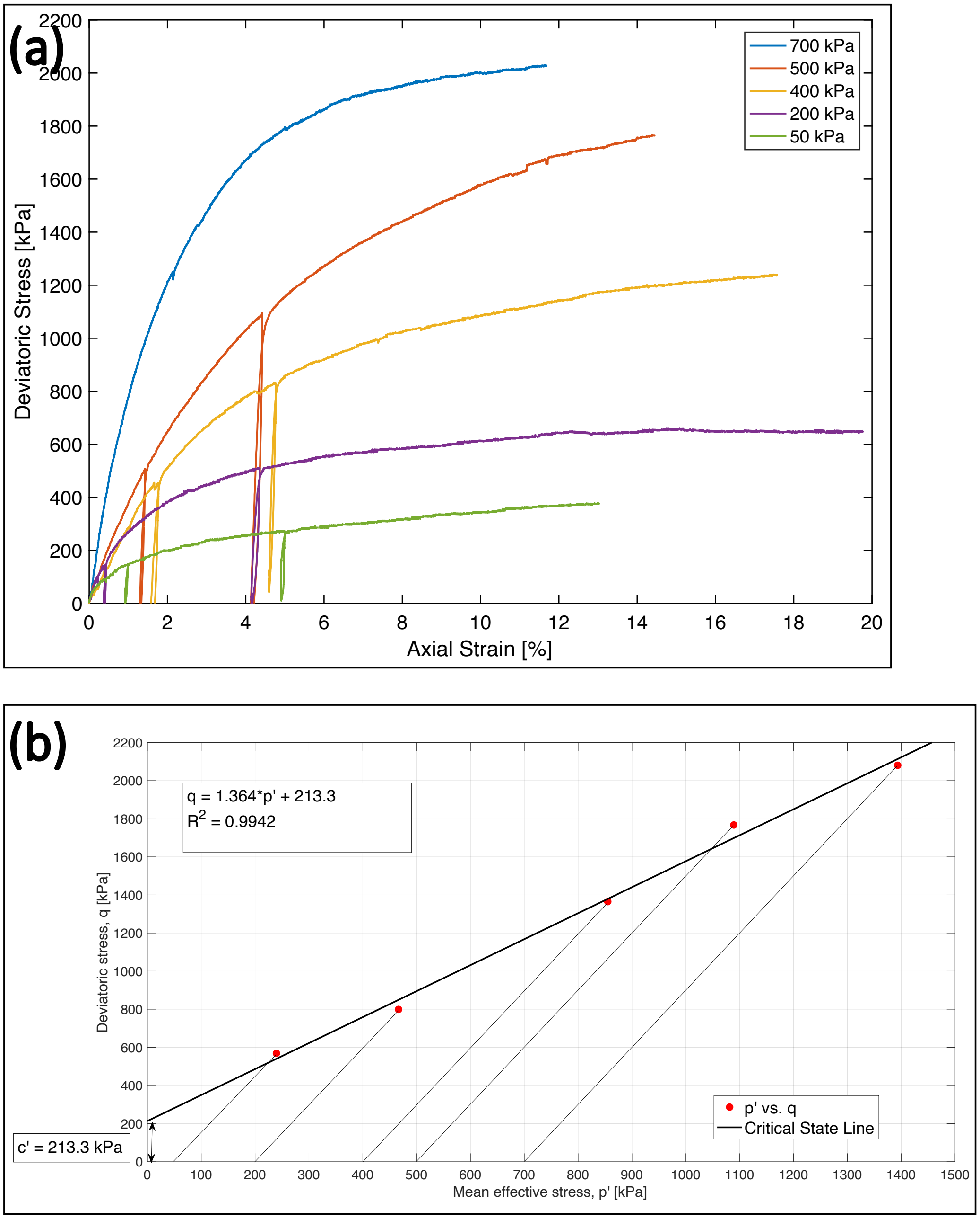

Figure 3: Meso-scale tests to characterize the critical state line of the material. (a) Axial strain [%] with deviatoric stress [kPa] of the triaxial tests performed on the landslide material at different confinement pressures. (b) Mean effective stress (p') [kPa] with deviatoric stress (q) [kPa] of each confinement pressure of Fig. 3a. The graph also shows the stress paths of each $p' - q$ point, the equation of the critical state line, the friction angle at the critical state (ϕ'), and the value of cohesion of the material (c').

First, a triaxial compression at the confinement of $200kPa$. When the radial compression has reached the value of $200kPa$ and holds the pressure, we have started the axial load with a velocity of $0.5mm/min$ with two loading-unloading cycles at 1 and 5% of axial strain (Fig. 4a). These two cycles of loading-unloading were performed to eliminate any inertia effects stemming from the frame's rigidity. We let the axial load continue, at a constant axial rate and constant confining pressure, until the sample reaches a critical state at which the deviatoric (differential) stress (q), confining stress, volume, pore pressure, and temperature remain constant (Fig. 4a). After these two cycles, the sample has let to reach a critical state until approximately 12% of axial strain, and the velocity stepping test starts. While at a critical state, velocity stepping is performed by increasing the axial load at five constant rates (i.e., velocities) from $0.0001 - 1mm/min$, allowing the sample to relax to a new critical state before performing the next velocity step (Fig. 4b). Through this exercise, the rate sensitivity of the material's shearing resistance at a critical state, q_{cs}, is evaluated to be:

$$q_{cs} = q_{ref} \left(\frac{V}{V_0} \right)^N \tag{1}$$

where V is the velocity $[mm/min]$, N is the rate sensitivity of the material $[-]$, q_{ref} and V_0 are the reference values for the shear resistance (deviatoric stress at critical state $[kPa]$) and the velocity $[mm/min]$, respectively. For the Silurian shales outside and inside the shear band, the parameters obtained from this part of the tests in all the samples are: $N = 0.0136$, $V_0 = 1mm/min$ and $q_{ref} = 719.4kPa$.

Once the velocity steps finish, the sample is kept at a critical state by holding its volume and allowing it to relax to the slowest critical state possible by the machine's specifications, at $V = 10^{-9} mm/min$. At this point, the thermal tests start (Fig. 4a) by keeping the confining pressure and loading velocity constant and only increasing the temperature slowly at steps of $2 - 3°C$, inducing a $1.5°c$ per hour rate, before letting it equilibrate to a new critical state for a couple of hours (Fig. 4c). The temperature of the sample was monitored with a thermal probe less than $10mm$ away from the sample, and the temperature was held constant until this probe stabilized to a steady state. Once the temperature of the sample and the axial stress are equilibrated, at each temperature variation, we mark the deviatoric stress values to obtain the thermal sensitivity of the material defined as:

$$q_{cs} = q_{ref} \exp\left(-M\Delta T\right) \tag{2}$$

where $\Delta T = T - T_{lab}$ is the temperature variation from the base value of $T_{lab} = 20°C$ and M is the thermal sensitivity coefficient $[°C^{-1}]$. For these tests we obtain $M = 0.04°C^{-1}$ and $q_{ref} = 719.4kPa$ for the material located at the center of the shear band. While at the edges of the shear band we have obtained $M = 0.023°C^{-1}$ and $q_{ref} = 695.15kPa$, and outside the shear band $M = 0.014°C^{-1}$ and $q_{ref} = 704.19kPa$.

5. Results

In this section, we show the results of the micro-and meso-scale tests performed on the core samples of the shear band of the Cal Ponet - Cal Borronet lobe. The micro-scale tests performed have also been previously presented by the authors (Seguí *et al.*, 2021). The meso-scale tests are presented below

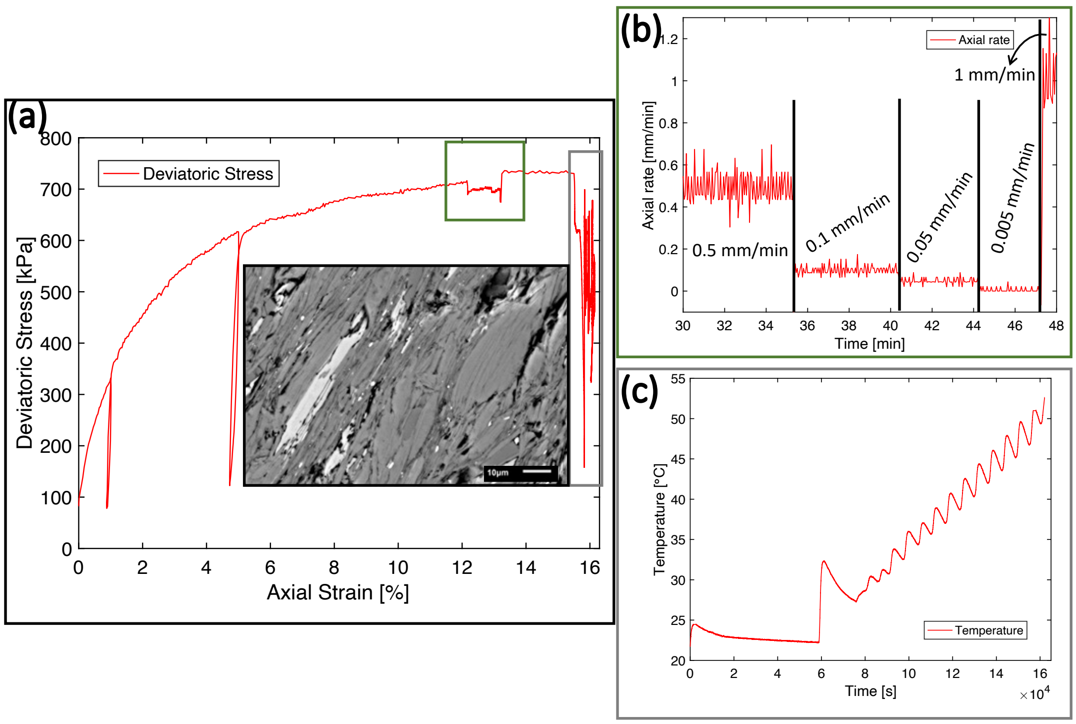

Figure 4: Experimental tests. (a) Graph of axial strain [%] and deviatoric stress, q $[kPa]$, showing the evolution of the axial load in isotropic compression with two axial load-unload cycles, velocity steps, and increase of temperature. The inlet is an SEM-EDS image of the shear band sample, showing the orientation of the phyllosilicates at the center of the shear band (muscovite [grey], chlorite [white], and paragonite [dark grey]) parallel to the shearing direction (Seguí *et al.*, 2021). (b) Graph of time $[min]$ with different axial rates $[mm/min]$ applied to all the tests performed. (c) Graph of time $[s]$ and the temperature of the sample $[°C]$ with an average increase of temperature of $1.5°C/hour$.

in detail, but part of them have been presented previously by the authors (Seguí & Veveakis, 2021).

5.1. Micro-scale tests

5.1.1. XRPD

A total of six samples have been tested in this study from the S10 borehole. From the XRPD tests, 5 mineral phases have been found: quartz [SiO_2], muscovite [$K_2Al_4Si_6Al_2O_{20}(OH,F)_4$], chlorite chamosite [$(Mg,Al,Fe)_{12}(Si,Al)_8O_{20}(OH)_{16}$], paragonite [$(K,Na)_2Al_4Si_6Al_2O_{20}(OH,F)_4$], and calcite [$CaCO_3$].

Fig. 5 presents the results of the quantitative analyses (in $wt\%$) of the mineral phases present in the six samples studied. The sample $27-27.5m$ is formed by quartz ($35wt\%$), muscovite ($52wt\%$), chlorite chamosite ($13wt\%$), and with minor presence of calcite ($\leq 1wt\%$). The rest of the samples analyzed by XRPD, present a very similar composition and proportion of the identified minerals, which are: $27.5-28m$, $28-28.5m$, $28.5-29m$, $29-29.5m$, and $29.5-30m$. In all the analyzed samples, the presence of quartz varies between 24 and $21wt\%$, muscovite between 59 and $53wt\%$, paragonite between 22 and $14wt\%$, and chlorite chamosite between 6 and 3%.

Therefore, the changes in the colors of the core samples seen in Fig. 1C are explained by the mineralogy. The sample $27-27.5m$, with high content in chlorite, presents a green tone, and samples from 28 to $30m$ depth have a high content in muscovite and paragonite which makes the material look darker (black-grey tones also influenced by the organic matter).

5.1.2. SEM-EDS

SEM-EDS analyses have confirmed the mineral composition of the phases found in the samples analyzed by XRPD. In the case of paragonite, EDS analyses reveal the presence of Na in the chemical composition. Moreover, phyllosilicate rich in potassium found is characterized as muscovite due to the amount of K in the mineral composition (Deer *et al.*, 1962). The samples analyzed from the S10 borehole represent the shear band and its surroundings showing four different textures as follows:

(i) Sample $27 - 27.5m$. This material is a black-gray-green shale with several small fractures - filled by quartz (Seguí *et al.*, 2021, Fig. 6) – surrounded by phyllosilicates (muscovite, paragonite, and chlorite). Muscovite particles are randomly oriented (Fig. 5) but show a fluidal texture of the platy grains of muscovite, with face-edge and face-face contacts. Quartz grains are found inside the sub-horizontal fractures with different thickness sizes between bands of phyllosilicates.

(ii) Sample $27.5 - 28m$. The texture of this sample is different from the rest. SEM-EDS images show large fragments of black-grey-green shales (Seguí *et al.*, 2021, Fig. 6) and, between them, small particles of quartz and phyllosilicates (muscovite, paragonite, and chlorite) with face-face and face-edge contacts. The texture inside the large clasts is identical to the texture of the $27-27.5m$ sample. These large fragments are not matrix-supported as the small particles of quartz and phyllosilicates are not attached (Fig. 5a,b).

(iii) Samples $28 - 28.5m$, $28.5 - 29m$, and $29.5 - 30m$. These samples are black-gray shale with small ($14\mu m$) and large (over $75\mu m$) fractures (filled by quartz), located between layers of phyllosilicates (muscovite, paragonite, and chlorite) and arranged forming folds. Phyllosilicate particles have a certain orientation and direction, following the shape of the folds (Fig. 5c,d), and their contacts are mainly face-edge, but with some face-face contacts. Quartz grains are located between phyllosilicates following the orientation of the folds (Seguí *et al.*, 2021, Fig. 6). In these samples, muscovite particles and chlorite-muscovite are present as intergrowths (Seguí *et al.*, 2021, Fig. 6) .

(iv) Sample $29 - 29.5m$ is where has been found the center of the shear band. It is a homogeneous and dark sample with large and oriented fractures filled with quartz. SEM-EDS images show a well-defined orientation and direction of the phyllosilicates -muscovite, paragonite, and chlorite- (Fig. 5e,f, and (Seguí *et al.*, 2021, Fig. 6)). This sample also presents thick fractures where, at their boundaries, the phyllosilicates are aligned (by their faces) parallel to the fractures (Seguí *et al.*, 2021, Fig. 6) . Furthermore, contacts between crystals of phyllosilicates are face-face (Seguí *et al.*, 2021, Fig. 6) .

The sizes of the phyllosilicates, in the analyzed samples, have been obtained by SEM-EDS, and vary between 6 and $50\mu m$.

5.1.3. MicroCT

Six samples of the S10 borehole have been tested to study the porosity of the material by MicroCT Scanning. The results are shown in Fig. 5, which presents the percentage of porosity of each sample, allow us to see the evolution of the porosity along with the shear band as follows:

(i) Samples $27-27.5m$, $27.5-28m$, and $28-28.5m$. These samples present a matrix volume fraction of 0.226, 0.2, and 0.23 and a porosity volume fraction of 0.0029, 0.0027, and 0.0027, respectively. Thus, the samples have a percentage of pores of 1.27%, 1.37%, and 1.15%, respectively (Fig. 5). The porosity in these samples have a defined orientation and direction of small pores as well as some large fractures (Seguí *et al.*, 2021, Fig. 7) .

(ii) Samples $28.5-29m$ and $29.5-30m$. These two samples have a matrix volume fraction of 0.14 and 0.22, and a porosity volume fraction of 0.00021 and 0.00019. Thus, with a percentage of pores in the sample of 0.14% and 0.087%, respectively (Fig. 5). The porosity in these samples is shown as very thin and large fractures, with an NW-SE direction (of the image (Seguí *et al.*, 2021, Fig. 7) , not the field), across the entire sample. Furthermore, the samples present small pores aligned and organized in bands, in the same direction and they look like thin fractures.

(iii) Sample $29-29.5m$. This sample presents a matrix volume fraction of 0.14 and a porosity volume fraction of 0.0033. Thus, with a percentage of pores in the sample of 2.16% (Fig. 5). This sample presents, at its center, a large fracture (Seguí *et al.*, 2021, Fig. 7) with large interconnected pores (where fluid can flow through them). This large fracture has an E-W direction (of the image (Seguí *et al.*, 2021, Fig. 7) , not the field). Above and below this fracture, there are thin fractures (some of them located at the bottom of the sample with larger pores) oriented parallel to the shear movement.

5.1.4. Plasticity Index

The plasticity index results are presented in relative values (i.e., all results are divided by the value obtained for the first sample, $27 - 27.5m$). We present the results in relative values because 1) the values obtained in Liquid Limit and Plastic Limit tests usually depend on the user, as each user adds a different amount of water to the samples; and 2) when the borehole was performed, the company obtained a plasticity index value of 8.7 for the sample $27.15 - 27.30m$ and now we obtained a plasticity value of 3.96 for the sample $27 - 27.5m$. This difference in the value of the plasticity index could also be due to the current dry state of the samples and their preservation after 12 years (since the borehole was performed). However, as the samples were uniformly exposed to the environment, we assume they degraded proportionally.

The results of the plasticity index reveal the same behavior as the porosity results (Fig. 5). These results show three distinct values that can be identified as three groups (same groups as MicroCT). Firstly, samples $27 - 27.5m$, $27.5 - 28m$, and $28 - 28.5m$, with values of relative plasticity index of 1, 0.93, and 0.97, respectively (Fig. 5). Secondly, samples $28.5 - 29m$ and $29.5 - 30m$, with relative plasticity values of 0.67 and 0.62, respectively (Fig. 5). The samples of the second group have lower values of relative plasticity index compared to the values of the first group (over 30% lower). And, thirdly, sample $29 - 29.5m$, has a value of relative plasticity index of 1.95 (Fig. 5), being a higher value of relative plasticity index compared to the rest of the samples.

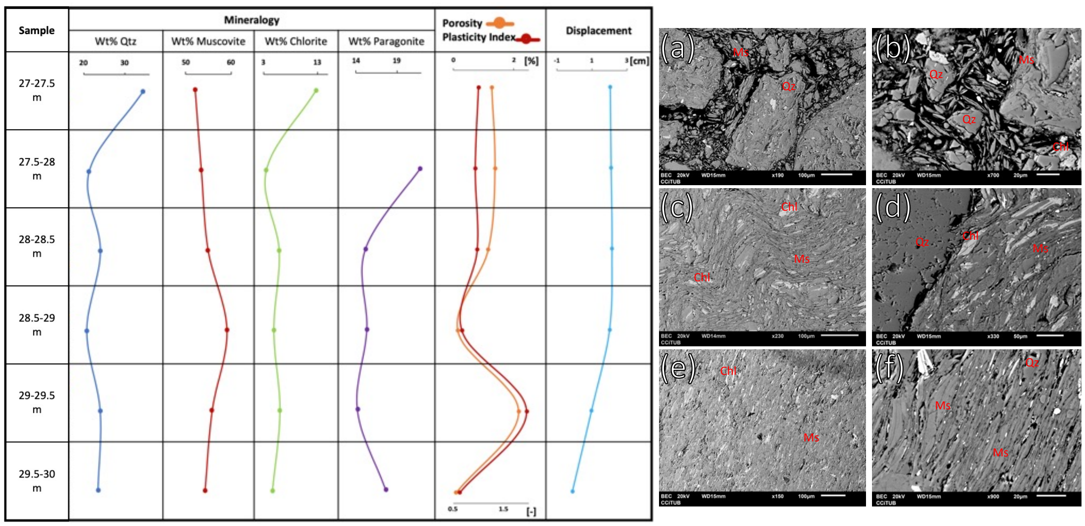

Figure 5: Results of the micro-scale tests. Mineral phases found by XRPD at each depth in $wt\%$, the porosity of each sample in %, and the relative plasticity index for each sample. Displacement data from the inclinometer (Fig. 1b, (EuroconsultSA, 2017)) is shown to correlate the results of the tests performed with the vertical deformation in the field. (a,b) SEM-EDS images of 27.5-28m sample, showing the randomly oriented and grain supported texture. (c,d) SEM-EDS images of 28.5-29m sample, showing the reorientation of the minerals forming smooth folds. (e,f) SEM-EDS images of 29-29.5m sample, showing the alignment of the minerals parallel to the shearing direction.

5.2. Meso-scale tests

The results obtained in this study, performed in the thermal triaxial with velocity stepping and temperature increase, are presented in Fig. 6a. The rate sensitivity for all the samples tested is the same for the Silurian shales of the S10 borehole of the Cal Ponet-Cal Borronet lobe. The data points of the rate sensitivity (axial rate - deviatoric stress at critical state) obtained for all the samples follows a power law. The equation of rate sensitivity obtained in this study is the following:

$$q_{cs} = 719.4 \cdot V^{0.0136} \tag{3}$$

where the value of rate sensitivity obtained for all the samples is $N = 0.0136$, for reference deviatoric stress of $q = 719.4kPa$ and reference velocity $V_0 = 1mm/min$.

Moreover, the data points for the three thermal sensitivities (outside, inside, and at the edges of the shear band) are presented in Fig. 6b. The tests on each sample have been carried out twice, as it was the maximum times that the material was able to be remolded, allowing thus to obtain more data points to determine with accuracy each equation law, which is the following:

$$q_{cs} = 704.19 \cdot e^{(-0.0136 \cdot \Delta T)} \tag{4}$$

$$q_{cs} = 695.15 \cdot e^{(-0.023 \cdot \Delta T)} \tag{5}$$

$$q_{cs} = 719.4 \cdot e^{(-0.04 \cdot \Delta T)} \tag{6}$$

where Eq. 4 refers to the thermal sensitivity outside the shear band with a value of $M = 0.0136$, Eq. 5 at the edges of the shear band with a value

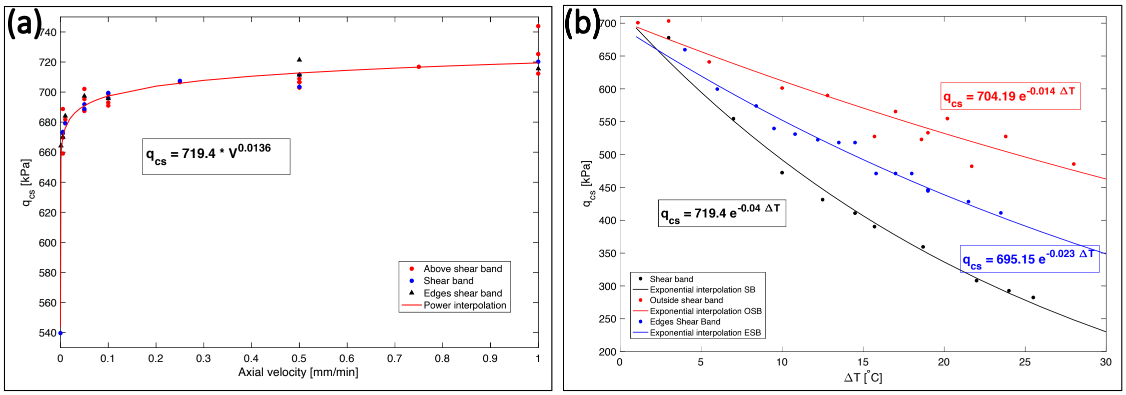

Figure 6: Results of the meso-scale tests. (a) Rate sensitivity of all the samples tested (outside, at the edges, and inside the shear band). The results obtained show the power law that represents the rate hardening behavior of the Silurian black shales. (b) Thermal sensitivities of outside (red), at the edges (blue), and inside (black) the shear band. The results follow exponential laws for each dataset that show the thermal softening behavior of the Silurian black shales within the area of the shear band.

of $M = 0.023$, and Eq. 6 at the center of the shear band with a value of $M = 0.04$, being the higher value of thermal sensitivity among all the samples tested.

6. Discussion

In this section, we discuss the validity of the experimental protocol performed on the thermal triaxial tests compared to other studies previously performed by other authors in clayey materials. Moreover, we interpret the results obtained at the meso-scale of thermal and rate sensitivities related to the fabric (orientation of the minerals) and the mineralogy of the samples tested at the micro-scale.

6.1. Validity of the experimental protocol

As we have mentioned previously in the Introduction section, Vardoulakis (2002b) presented a mathematical model for the thermal and rate behavior of clayey shear bands, that accounts for thermal softening and rate hardening of the material when shearing. In this mathematical model the author couples the thermo- and visco-plastic behavior of the clays. In that paper, the laboratory results presented were from Leinenkugel (1976), who performed tests on remolded kaolin clay to obtain the strain-rate sensitivity, and Hicher (1974) that performed tests on black clay (kaolinite) to obtain the thermal friction sensitivity of the material. Leinenkugel (1976) obtained the power law of Eq. (1) to describe the shear stress behavior with the strain-rate and the rate sensitivity of the material, which is a rate hardening law (i.e., when increasing the velocity/strain-rate, the shear stress increases). Leinenkugel (1976) obtained a value of rate sensitivity for kaolin of $N = 0.01$ (Table 1). Rate sensitivity data from other authors is also presented in Fig. 7a, showing the same power law and rate hardening, the same as the one obtained in this study. Samuelson & Spiers (2012) performed direct shear with velocity stepping in fault gouges material formed by high content on illite (Fig. 7a), with a value of rate sensitivity of $N = 0.0079$ (Table 1). Ikari *et al.* (2009) performed velocity stepping tests in a biaxial stressing apparatus on a synthetic montmorillonite-rich gouge (Fig. 7a), obtaining a value of rate sensitivity of $N = 0.0116$ (Table 1).

Regarding thermal sensitivity, Hicher (1974) performed triaxial tests to see the evolution of the material with temperature. The latter obtained a thermal softening behavior of the clayey material (i.e., when the temperature increases, the residual friction coefficient of the material decreases), with the result of the exponential law of Eq. (2). This exponential law defines the residual friction coefficient as the reference friction coefficient by the exponential thermal sensitivity of the material and the difference between actual and reference temperatures. Hicher (1974) obtained a value of thermal sensitivity for kaolinite of $M = 0.0093°C^{-1}$ (Table 1). Additional data of thermal sensitivity from other authors is shown in Fig. 7b, where the law is the same exponential law as Hicher (1974) obtained, and is the same as the one obtained in this study, showing a thermal softening of the clayey materials. Robinet, J.-C. *et al.* (1997) performed thermal test in a oedometer on kaolinite (Fig. 7b), with a thermal sensitivity value of $M = 0.021°C^{-1}$ (Table 1). Hueckel *et al.* (2009) performed temperature increase in triaxial tests on carbonate clays (Hueckel *et al.*, 1998), with a value of thermal sensitivity of $M = 0.003°C^{-1}$ (Fig. 7b, Table1).

As shown in Fig. 7, the results of the tests performed in the customized thermal triaxial for the Silurian black shales of the Cal Ponet-Cal Borronet lobe, allowed us to obtain the same laws for thermal and rate sensitivities as the aforementioned authors for different types of clayey materials. The values of thermal and rate sensitivities are within the range of the ones obtained from the other experiments presented in Fig. 7. Thus, by performing both types of tests (velocity stepping and temperature increase) on the same sample, due to the limitation of core material, we have been able to obtain accurate values.

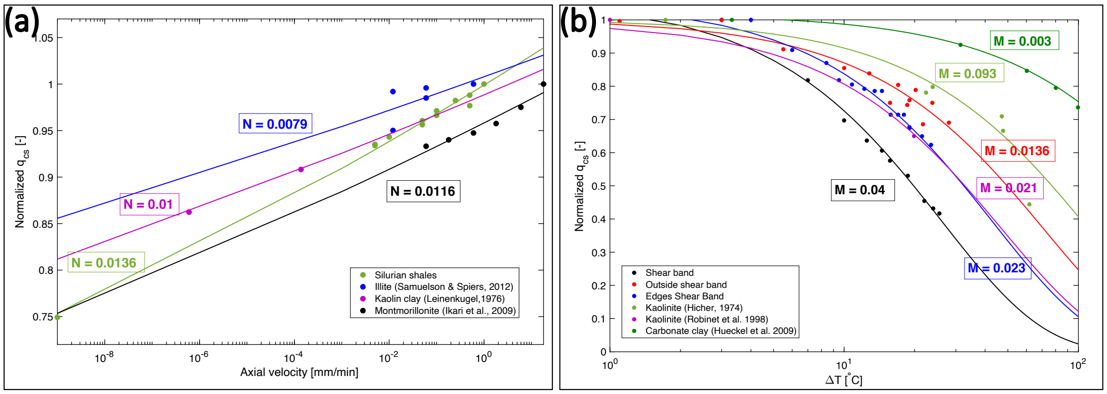

Figure 7: Validity of the meso-scale tests. (a) Comparison of rate sensitivity values obtained in this study by velocity stepping with other velocity stepping tests performed on clayey materials by other authors. Showing the values of rate sensitivity for each test and the rate hardening results. (b) Comparison of thermal sensitivity values obtained in this study by temperature increase with other thermal increase tests performed on clayey materials by other authors. Showing the values of thermal sensitivity for each test and the thermal softening results.

Table 1: Values of rate and thermal sensitivities. Reference deviatoric stress at critical state $q_{cs}ref$, thermal sensitivity M, and rate sensitivity N. The values of this table are the ones obtained from the rate and thermal laws shown in Fig. 7.

q_{cs} ref [kPa]	M [˚C^{-1}]	N [-]	Material
719.4		0.0136	Silurian shales
719.35		0.0079	Illite (after Samuelson & Spiers 2012)
691.88		0.0095	Kaolin clay (after Leinenkugel, 1976)
719.54		0.0116	Montmorillonite (after Ikari et al., 2009)
719.4	0.04		Silurian shales (shear band)
704.19	0.014		Silurian shales (outside the shear band)
695.15	0.023		Silurian shales (edges of the shear band)
719.4	0.0093		Kaolinite (after Hicher, 1974)
719.4	0.021		Kaolinite (after Robin et al., 1998)
719.4	0.003		Carbonate clay (after Hueckel et al., 2009)

6.2. Relationship between mineralogy and fabric with rate and thermal sensitivity

The results of the meso-scale tests have revealed the same rate sensitivity value of the material for all the samples tested. These results could be explained by the six samples having the same mineralogy, despite their variations in $wt\%$ of each mineral phase (Fig. 8). All the samples are, overall, composed of the same three phyllosilicates (chlorite, muscovite, and paragonite) and quartz. It can be seen, in Fig. 8, that the variation of the amount of quartz vs. phyllosilicates does not affect the rate sensitivity of the material. By comparing the values of the rate sensitivity of the Silurian black shales with the other clayey materials in Fig. 7a can be seen that most of them have very similar values, but their difference could be due to their content in additional mineral phases and higher difference in $wt\%$.

Thermal sensitivity results show different values for different depths of the samples tested (Fig. 6b). This difference could indicate that it is due to the effect of the fabric of each sample. The orientation of the mineralogy with face-face contacts shows a higher value of thermal sensitivity of the material. Whereas, when the material is randomly oriented with face-edge and/or edge-edge contacts, the thermal sensitivity is the lowest one. The results also show an intermediate value of thermal sensitivity for the samples right above and below the center of the shear band. This seems to be due to an intermediate rearrangement of the minerals (as they are oriented in smoother folds). Fig. 8 correlates the effect of the fabric in terms of porosity and plasticity index with the thermal sensitivity of each sample, showing almost the same behavior between them. This correlation of the fabric with porosity is because the porosity outside the shear band is randomly oriented with an average value of % of pores, at the edges of the shear band the material becomes more oriented with smoother folds that induce lower porosity and smaller pores due to the start of this rearrangement in the form of smooth folds, and at the center of the shear band the full alignment of the phyllosilicates parallel to the shearing direction rearranges mechanically the pores by creating a path of connected pores with the highest % of porosity. Moreover, we can also correlate the fabric of the samples with the plasticity index due to the contact edge-face and/or edge-edge are the stronger ones that make the material less susceptible to friction (i.e., less plastic -a lower value of plasticity index-), whereas the contacts face-face that we found at the center of the shear band are the weakest contacts, thus, facilitating the friction (i.e., more plastic - higher plasticity index). Also, the plasticity index is correlated with the porosity, as outside the shear band we have a higher value of plasticity index due to higher pores in the sample (i.e., allowing the material to absorb more water), while at the edges of the shear band and regardless of the rearrangement of the mineralogy in smoother folds, the material has lower porosity with smaller pores, which causes the material to absorb less water, hence being less plastic. Finally, at the center of the shear band, the minerals are completely aligned but also we found higher porosity with pores interconnected creating a channel that allows us to absorb more water.

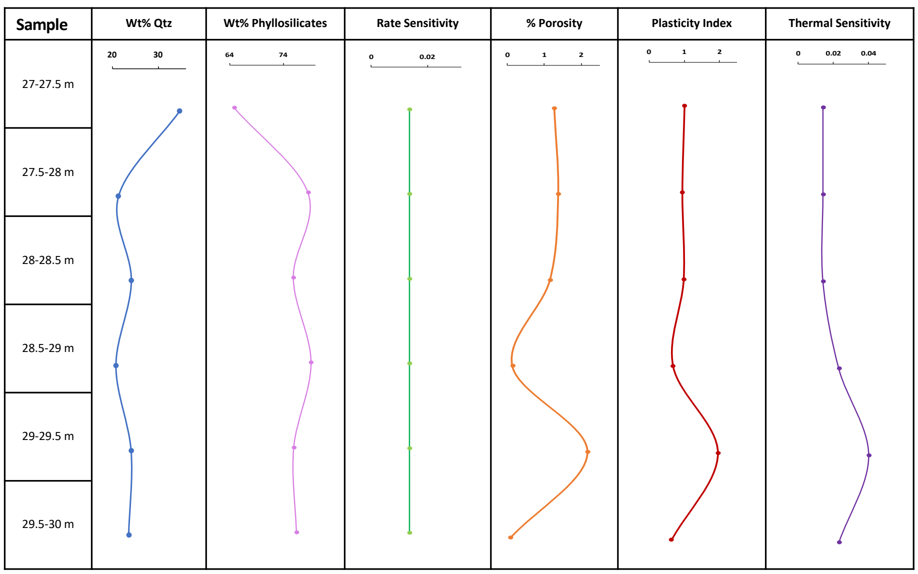

Figure 8: Correlation of the micro-and meso-scale tests. Evolution in depth of the $\%wt$ of quartz and phyllosilicates with values of rate sensitivity of each sample. Also, the table correlates in depth the evolution of % of porosity and plasticity index with the thermal sensitivity.

7. Conclusions

This paper presents a micro-and meso-scale study of the Silurian black shales of the shear band area of a deep-seated landslide, the Cal Ponet-Cal Borronet lobe inside the El Forn landslide in Andorra. The results of the micro-scale tests (XRPD, SEM-EDS, MicroCT, and plasticity index) show that, while the mineral phases do not change from outside to inside the shear band, the fabric (orientation of the minerals) does by being randomly oriented outside to completely aligned parallel to the shearing direction in the shear band. This reorganization of the mineralogy affects the porosity, from being non-connected outside the shear band to interconnected forming a layer of porosity inside the shear band. The effect of the alignment of the minerals with face-face contacts also increases the plasticity index of the material.

Moreover, the meso-scale results of the experimental tests performed in the thermal triaxial machine show that the Silurian black shales have the same rate sensitivity, being the material rate hardening, regardless of their location (inside or outside the shear band). However, the thermal sensitivity results show different values, depending on the location of the sample (outside, inside, or at the edges of the shear band), with thermal softening in all of them.

All these results have allowed us to associate the rate and thermal behavior of the material with the mineralogy and the fabric of the samples. The rate sensitivity is directly dependent on the mineral phases present in the material, while the thermal sensitivity of the material is correlated with the fabric of the sample, by being more thermal sensitive when the minerals are completely aligned in one direction and with face-face contacts, while less thermal sensitive when the minerals are randomly oriented with face-edge or edge-edge contacts.

Furthermore, the newly experimental protocol followed in the present study has shown that both, the thermal and rate tests, can be performed on a single sample. This allows to optimize the amount of material and obtain more data, especially when there is limited material from a borehole. We have also validated the results of this experimental protocol by comparing it to previous studies that have performed velocity stepping tests and temperature increase tests, separately, on clayey materials. Showing that the values obtained in the present study are very similar to the other experimental tests from several authors.

This paper, thus, shows the importance of the thermal and rate sensitivity of the material in the shear band of a deep-seated landslide, regarding the fabric and mineralogy, respectively. These parameters are important to consider when studying shear zones and the stability of natural hazards and how the thermal and rate sensitivities evolve when the material experiences friction/shearing movements.

Conflict of interest

The authors declare that they have no conflict of interest.

Acknowledgements

XRPD and SEM-EDS (http://www.ccit.ub.edu/ES/tm02.html) analysis were made and performed at the Scientific and Technological Centers of the University of Barcelona (CCiTUB). Thin sections were made at the "Servei de Làmina prima" from the Faculty of Earth Sciences at Barcelona University. MicroCT tests were carried out at the Duke University Shared Materials Instrumentation Facility (SMIF), a member of the North Carolina Research Triangle Nanotechnology Network (RTNN), which is supported by the National Science Foundation (Grant ECCS-1542015) as part of the National Nanotechnology Coordinated Infrastructure (NNCI). Liquid and plastic limit tests were carried out at the Soil Mechanics laboratory at Duke University. The authors acknowledge the help of the laboratory technician Michael Blagg in performing the plasticity index tests. The rate and thermal triaxial tests were carried out at the Multiphysics Geomechanics Laboratory at Duke University. Support by the NSF CMMI-2006150 and CMMI-2042325 projects, and PID2019-105625RB-C21 funded by MCIN/ AEI/10.13039/501100011033/ are also acknowledged.

References

Alevizos, S., Poulet, T., & Veveakis, E. 2014. Thermo-poro-mechanics of chemically active creeping faults. 1: Theory and steady state considerations. *Journal of Geophysical Research: Solid Earth*, **119**(6), 4558–4582.

Alonso, E. E., Zervos, A., & Pinyol, N. M. 2016. Thermo-poro-mechanical analysis of landslides: from creeping behaviour to catastrophic failure. *Géotechnique*, **66**(3), 202–219.

Anderson, D. L. 1980. An earthquake induced heat mechanism to explain the loss of strength of large rock and earth slides. *Pages 569–580 of:* Wiley, John (ed), *In Proceedings of the International Conference on Engineering for Protection from Natural Disasters*.

Bruker. 2007. *X-ray diffraction software*. Tech. rept. Diffrac Plus Evaluation Software.

Cecinato, Francesco, & Zervos, Antonis. 2012. Influence of thermomechanics in the catastrophic collapse of planar landslides. *Canadian Geotechnical Journal*, **49**(2), 207–225.

Cecinato, Francesco, Zervos, Antonis, & Veveakis, Emmanuil. 2010. A thermo-mechanical model for the catastrophic collapse of large landslides. *International Journal for Numerical and Analytical Methods in Geomechanics*, **35**(14), 1507–1535.

Chambon, Guillaume, Schmittbuhl, Jean, & Corfdir, Alain. 2002. Laboratory gouge friction: Seismic-like slip weakening and secondary rate- and state-effects. *Geophysical Research Letters*, **29**(10), 4–1–4–4.

Ciantia, M.O., & Hueckel, T. 2013. Weathering of submerged stressed calcarenites: chemo-mechanical coupling mechanisms. *Géotechnique*, **63**(9), 768–785.

Clariana, P. 2004. *El sinclinori de Tor-Casamanya. Estudi estratigràfic i estructural, Nova cartografia geológica a escala 1:25000*. Tech. rept. Horitzó 6:3–15. Rev Centre Recerca Ciènc Terra.

Coelho, A. A. 2000. Whole-profile structure solution from powder diffraction data using simulated annealing. *Journal of Applied Crystallography*, **33**(3), 899–908.

Corominas, Jordi, Iglesias, Rubén, Aguasca, Albert, Mallorqui, Jordi, Fabregas, Xavier, Batlle, Xavier, & Gili, Josep. 2014 (09). Comparing Satellite Based and Ground Based Radar Interferometry and Field Observations at the Canillo Landslide (Pyrenees). *In: IAEG XII CONGRESS Proceedings*, vol. 2.

Das, B.M. 1941. *Soil mechanics: laboratory manual*. Vol. 8th edition. Oxford University Press.

Deer, W A, Howie, R A, & Zussman, J. 1962. *An Introduction to the Rock-Forming Minerals*. Prentice Hall.

Del Olmo, C., Fioravante, V., Gera, F., Hueckel, T., Mayor, J.C., & Pellegrini, R. 1996. Thermomechanical properties of deep argillaceous formations. *Engineering Geology*, **41**(1), 87–102.

EuroconsultSA. 2017. *Auscultacions inclinomètriques, piezomètriques i extensomètriques al moviment de massa del Forn*. Tech. rept. Ref. U-1586-A23.

Gens, Antonio, Wieczorek, Klaus, Gaus, Irina, Garitte, Benoit, Mayor, Juan Carlos, Schuster, Kristof, Armand, Gilles, García-Siñeriz, José Luis,

& Trick, Thomas. 2018. *Performance of the Opalinus Clay under thermal loading: experimental results from Mont Terri rock laboratory (Switzerland)*. Cham: Springer International Publishing. Pages 271–288.

Goren, L., & Aharonov, E. 2007. Long runout landslides: The role of frictional heating and hydraulic diffusivity. *Geophysical Research Letters*, **34**(7).

Hicher, P. Y. 1974. *Etude des proprietes mecaniques des argiles a l' aide d' essais triaxiaux, influence de la vitesse et de la temperature, Report of the soil mechanics laboratory,*. Tech. rept. Ecole Central, de Paris.

Hueckel, T., & Baldi, G. 1990. Thermoplasticity of Saturated Clays: Experimental Constitutive Study. *Journal of Geotechnical Engineering*, **116**(12), 1778–1796.

Hueckel, T., & Borsetto, M. 1990. Thermoplasticity of Saturated Soils and Shales: Constitutive Equations. *Journal of Geotechnical Engineering*, **116**(12), 1765–1777.

Hueckel, T., & Pellegrini, R. 1991. Thermoplastic modeling of undrained failure of saturated clay due to heating. *Soils and Foundations*, **31**(3), 1–16.

Hueckel, T., & Pellegrini, R. 1992. Effective stress and water pressure in saturated clays during heating–cooling cycles. *Canadian Geotechnical Journal*, **29**(6), 1095–1102.

Hueckel, T., François, B., & Laloui, L. 2009. Explaining thermal failure in saturated clays. *Géotechnique*, **59**(3), 197–212.

Hueckel, Tomasz, Pellegrini, Rita, & Del Olmo, Carlos. 1998. A constitutive study of thermo-elasto-plasticity of deep carbonatic clays. *International Journal for Numerical and Analytical Methods in Geomechanics*, **22**(7), 549–574.

Ikari, Matt J., Saffer, Demian M., & Marone, Chris. 2009. Frictional and hydrologic properties of clay-rich fault gouge. *Journal of Geophysical Research: Solid Earth*, **114**(B5).

Kohli, Arjun, & Zoback, Mark. 2013. Frictional properties of shale reservoir rocks. *Journal of Geophysical Research: Solid Earth*, **118**(09).

Lachenbruch, Arthur H. 1980. Frictional heating, fluid pressure, and the resistance to fault motion. *Journal of Geophysical Research: Solid Earth*, **85**(B11), 6097–6112.

Laloui, L., & Cekerevac, C. 2003. Thermo-plasticity of clays. *Computers and Geotechnics*, **30**(8), 649–660.

Laloui, Lyesse. 2001. Thermo-mechanical behaviour of soils. *Revue Française de Génie Civil*, **5**(6), 809–843.

Leinenkugel, H.-J. 1976. *Deformations und Festigkeitverhalten bindiger Erdstoffe: Experimental Ergebnisse und ihre physikalische Deutung*. Ph.D. thesis, Karlsruhe University, Karlsruhe, Germany.

Mase, Charles W., & Smith, Leslie. 1985. Pore-fluid pressures and frictional heating on a fault surface. *Pure and Applied Geophysics PAGEOPH*, **122**(2-4), 583–607.

Monfared, Mohammad, Sulem, Jean, Delage, Pierre, & Mohajerani, Mehrdokht. 2014. Temperature and Damage Impact on the Permeability of Opalinus Clay. *Rock Mechanics and Rock Engineering*, **47**(1), 101–110.

Pinyol, Núria M., & Alonso, Eduardo E. 2010. Criteria for rapid sliding II.: Thermo-hydro-mechanical and scale effects in Vaiont case. *Engineering Geology*, **114**(3), 211 – 227.

Poulet, T., Veveakis, E., Regenauer-Lieb, K., & Yuen, D. A. 2014. Thermo-poro-mechanics of chemically active creeping faults: 3. The role of serpentinite in episodic tremor and slip sequences, and transition to chaos. *Journal of Geophysical Research: Solid Earth*, **119**(6), 4606–4625.

Rattez, Hadrien, & Veveakis, Manolis. 2020. Weak phases production and heat generation control fault friction during seismic slip. *Nature Communications*, **11**(1), 350.

Rattez, Hadrien, Stefanou, Ioannis, Sulem, Jean, Veveakis, Manolis, & Poulet, Thomas. 2018. The importance of Thermo-Hydro-Mechanical couplings and microstructure to strain localization in 3D continua with application to seismic faults. Part II: Numerical implementation and post-bifurcation analysis. *Journal of the Mechanics and Physics of Solids*, **115**, 1–29.

Rice, James R. 2006. Heating and weakening of faults during earthquake slip. *Journal of Geophysical Research: Solid Earth*, **111**(B5), n/a–n/a.

Robinet, J.-C., Pasquiou, A., Jullien, A., Belanteur, N., & Plas, F. 1997. Expériences de laboratoire sur le comportement thermo-hydro-mécanique de matériaux argileux remaniés gonflants et non gonflants. *Rev. Fr. Geotech.*, 53–80.

Samuelson, Jon, & Spiers, Christopher J. 2012. Fault friction and slip stability not affected by Co2 storage: Evidence from short-term laboratory experiments on North Sea reservoir sandstones and caprocks. *International Journal of Greenhouse Gas Control*, **11**, S78–S90. CATO: CCS Research in the Netherlands.

Santamarina, J., & Cho, Gye-Chun. 2001. Determination of Critical State Parameters in Sandy Soils—Simple Procedure. *Geotechnical Testing Journal*, **24**(06), 185–192.

Sari, Mustafa, Alevizos, Sotiris, Poulet, Thomas, Lin, Jack, & Veveakis, Manolis. 2020. A visco-plastic framework for interface processes in sedimentary reservoir rocks at HPHT conditions. *Geomechanics for Energy and the Environment*, **22**, 100165.

Seguí, Carolina, & Veveakis, Manolis. 2021. Continuous assessment of landslides by measuring their basal temperature. *Landslides*, **18**(12), 3953–3961.

Seguí, Carolina, & Veveakis, Manolis. 2022. Forecasting and mitigating landslide collapse by fusing physics-based and data-driven approaches. *Geomechanics for Energy and the Environment*, **32**, 100412.

Seguí, Carolina, Rattez, Hadrien, & Veveakis, Manolis. 2020. On the Stability of Deep-Seated Landslides. The Cases of Vaiont (Italy) and Shuping (Three

Gorges Dam, China). *Journal of Geophysical Research: Earth Surface*, **125**(7).

Seguí, Carolina, Tauler, Esperança, Planas, Xavier, Moya, Jose, & Veveakis, Manolis. 2021. The interplay between phyllosilicates fabric and mechanical response of deep-seated landslides. The case of El Forn de Canillo landslide (Andorra). *Landslides*, **18**(1), 145–160.

Song, Kun, Yan, Echuan, Zhang, Guodong, & Yi, Qinglin. 2014. Back Analysis of Hydraulic Properties for a Landslide in the Three Gorges Area. *Advances in Transportation Geotechnics and Materials for Sustainable Infrastructure*, Jun.

Sulem, Jean, Stefanou, Ioannis, & Veveakis, Emmanuil. 2011. Stability analysis of undrained adiabatic shearing of a rock layer with Cosserat microstructure. *Granular Matter*, **13**(3), 261–268.

Tesei, Telemaco, Collettini, Cristiano, Carpenter, Brett, Viti, Cecilia, & Marone, Chris. 2012. Frictional strength and healing behavior of phyllosilicate-rich faults. *Journal of Geophysical Research (Solid Earth)*, **117**(09), 9402–.

TJP. 2015. *Avizo Guide. Avizo training materials.* BRC-Imaging Facility.

Vardoulakis, I. 2002a. Dynamic thermo-poro-mechanical analysis of catastrophic landslides. *Géotechnique*, **52**(3), 157–171.

Vardoulakis, I. 2002b. Steady shear and thermal run-away in clayey gouges. *International Journal of Solids and Structures*, **39**(13), 3831 – 3844.

Veveakis, E., & Regenauer-Lieb, K. 2015. Cnoidal waves in solids. *Journal of the Mechanics and Physics of Solids*, **78**, 231 – 248.

Veveakis, E., Alevizos, S., & Vardoulakis, I. 2010. Chemical reaction capping of thermal instabilities during shear of frictional faults. *Journal of the Mechanics and Physics of Solids*, **58**(9), 1175 – 1194.

Veveakis, E., Poulet, T., & Alevizos, S. 2014. Thermo-poro-mechanics of chemically active creeping faults: 2. Transient considerations. *Journal of Geophysical Research: Solid Earth*, **119**(6), 4583–4605.

Veveakis, Emmanuil, Vardoulakis, Ioannis, & Di Toro, Giulio. 2007. Thermoporomechanics of creeping landslides: The 1963 Vaiont slide, northern Italy. *Journal of Geophysical Research*, **112**(F3).

Voight, B., & Faust, C. 1982. Frictional heat and strength loss in some rapid landslides. *Géotechnique*, **32**(1), 43–54.

Wang, Ding-Jian, Tang, Hui-Ming, Zhang, Ya-Hui, Li, Chang-Dong, & Huang, Lei. 2017. An improved approach for evaluating the time-dependent stability of colluvial landslides during intense rainfall. *Environmental Earth Sciences*, **76**(8).